Microstructure and texture evolution during the manufacturing of in situ TiC-NiCr cermet through selective laser melting process

Atefeh Aramian[a], Zohreh Sadeghian[a,*] z.sadeghian@scu.ac.ir, Di Wan[b], Yaroslav Holovenko[c], Seyed Mohammad Javad Razavi[b], Filippo Berto[b]

[a]Department of Material Science and Engineering, Faculty of Engineering, Shahid Chamran University, Golestan Boulevard, 6135785311 Ahvaz, Iran
[b]Department of Mechanical and Industrial Engineering, Norwegian University of Science and Technology (NTNU), Richard Birkelans vei 2b, 7491 Trondheim, Norway
[c]Department of Mechanical and Industrial Engineering, Tallinn University of Technology, Ehitajate Tee 5, 19086, Tallinn, Estonia

[*]Corresponding author.

Abstract

The effects of different selective laser melting (SLM) scan speeds (150 mm$\cdot$s^{-1}, 95 mm$\cdot$s^{-1}, 60 mm$\cdot$s^{-1}, 55 mm$\cdot$s^{-1}, and 50 mm$\cdot$s^{-1}) on the microstructure and texture evolution of in situ TiC-NiCr cermet were investigated in the present study. The rotating scan strategy of 60° rotation (Rot-scan) was used to print the samples. Microstructural evolutions were investigated using scanning electron microscopy (SEM). Electron backscatter diffraction (EBSD) and X-ray diffraction analyses were used to identify the micro- and macro-crystallographic preferred orientation (texture). According to the results, the in situ formation of TiC via exothermic reaction resulted in different directions of temperature gradient in the melt pool. Consequently, nucleation and growth occurred in various directions. However, α-fiber texture could be observed in the orientation distribution function (ODF) of the manufactured specimens.

Keywords: Additive manufacturing (AM); Selective laser melting (SLM); Electron backscatter diffraction (EBSD); Macro-micro texture; TiC-based cermet

1. Introduction

Selective laser melting (SLM) belongs to the category of laser powder bed fusion (LPBF) additive manufacturing (AM) process, which is capable of manufacturing parts with complex geometries [1]. High-speed repetitive heating and cooling cycles together with temperature gradient during the SLM process often result in a heterogeneous and anisotropic microstructure in the manufactured specimens [2–4]. Generally, microstructural anisotropy in SLM specimens is associated with coarse columnar grains with preferential crystal orientations along the printing direction. As a result of temperature gradients, the nucleation rate at the solidification front is lowered, and thus, promoting epitaxial grain growth is the preferred mechanism of solidification during SLM [4]. Consequently, grain morphology and crystallographic texture cause anisotropic mechanical properties. Structural properties (crystallographic structure, phase transformation, and phase distribution), and SLM process parameters such as power, scanning speed, and scanning strategy can affect the texture evolution in SLM samples. Despite the broad range of literature on texture development during SLM, the mechanism of texture evolutions has still not been sufficiently clarified. Song et al. [2] reported a columnar microstructure with <100> texture (corresponding to (200) plane) oriented along the building direction in NiCr alloy samples manufactured through SLM. They observed that microstructural anisotropy decreased with increase in laser scanning speed.

In recent years, many efforts have been made to widen the range of materials used in additive manufacturing, including polymers, metals, ceramics, and their combinations, such as cermet materials [5,6]. Cermets, as one of the challenging materials for printing, are composite materials that combine the desirable toughness and thermal conductivity of metals with the high hardness, excellent wear resistance, and oxidation resistance of ceramics [7,8]. Moreover, cermets are a promising option for use in high-temperature applications. In recent decades, tungsten carbide-cobalt (WC-Co) was developed and successfully used as a material for producing cutting tools [9]. Nevertheless, practical applications of WC-Co cermets have been limited due to their insufficient oxidation and corrosion resistance and constrained high-temperature plastic deformation, and the relatively high price of Co [10,11]. Various combinations of ceramic particles and metal binders have been established to enhance corrosion and oxidation resistance and to replace Co with reasonable elements. TiC-based cermets have gained considerable attention because of their lower density and higher corrosion resistance compared to conventional hard metals (WC-Co) [12,13].

During the last decade, different possible methods have been used to characterize the texture. The most common and advantageous techniques for measuring crystallographic texture are X-ray diffraction (XRD) and electron backscattered diffraction (EBSD). XRD texture measurements seem to be more accurate due to the large area of scanning (a whole part of the sample), and the absence of microstructural evidence in the X-ray measurements makes EBSD preferable concerning microstructure and texture analysis. Nevertheless, both of these techniques provide reliable results for texture analysis. Hence, choosing the most suitable technique depends on the sample manufacturing procedure [14].

In the present research, the effects of scan speed variation (different input energy densities) on the microstructure and texture evolution of the in situ TiC-NiCr cermet fabricated through SLM process were evaluated. For this purpose, the macro- and micro-crystallographic texture of bulk samples were studied through XRD and EBSD analyses.

2. Materials and methods

Commercially available Ti (98.9%; spherical; ≤ 45 µm), amorphous C (99.95%; spherical; 2-12 µm), and $Ni_{80}Cr_{20}$ (near-spherical; ≈ 20 µm) were used as feedstock to produce TiC-40 wt. % NiCr cermet through SLM. The powder preparation process was conducted in two steps. Ti and carbon powder were first mixed for 5 hours and milled at a rotating speed of 350 rpm in isopropanol using a high-speed milling machine (Retch, E max, Germany). In the second step, Ti and C powder were mixed with NiCr powder for 10 hours in isopropanol using a convectional mixing machine.

Cylindrical samples of 5 mm diameter and 6 mm height were printed with the following process parameters: power of 62.4 W, layer thickness of 50 µm, hatch spacing of 60 µm, and scan speeds of 150, 95, 60, 55, and 50 $mm.s^{-1}$. Specimens were fabricated perpendicular to the SLM platform. Scan lines of each layer were turned 60° relative to the previous layer, as shown schematically in Fig. 1.

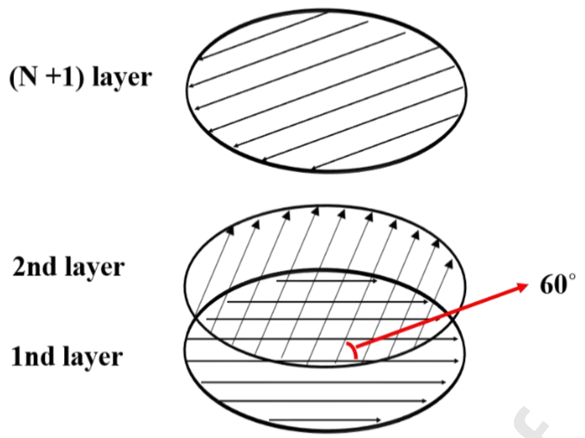

Fig. 1. Schematic illustration of the scanning pattern

Phase analysis of feedstock milled powder and SLM processed samples was conducted using an X-ray diffractometer (D8 A25 DaVinci; Bruker Optics Inc., Billerica, MA, USA) with CuK$_\alpha$ radiation (λ = 0.15406 nm). The microstructure was evaluated using field emission scanning electron microscopy (FESEM; Ultra 55 Ltd.; Zeiss, Oberkochen, Germany) using the backscattered electron (BSE) mode. The crystallographic texture of the fabricated parts was investigated through XRD and SEM using EBSD analysis on both top and side views (Fig. 2). Moreover, OIM software was used to analyze the EBSD data.

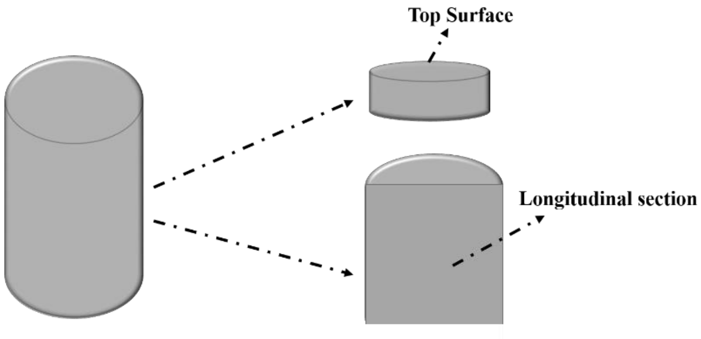

Fig. 2. Schematic illustration of the analyzed surface of the samples

3. Result and discussion

3.1 Phase evolution

XRD pattern of the feedstock power after milling process and SLM process is depicted in Fig.3. There is no sign of Ti-C reaction during the mixing procedure (Fig. 3-a). XRD patterns of the specimens manufactured with various scan speeds revealed that Ti-C reaction occurred during the SLM process which results in TiC phase formation. In addition, weak peaks of Ni_3Ti has emerged after SLM process (Fig. 3-b). The mechanism of TiC phase formation has been previously discussed in detail [15][6].

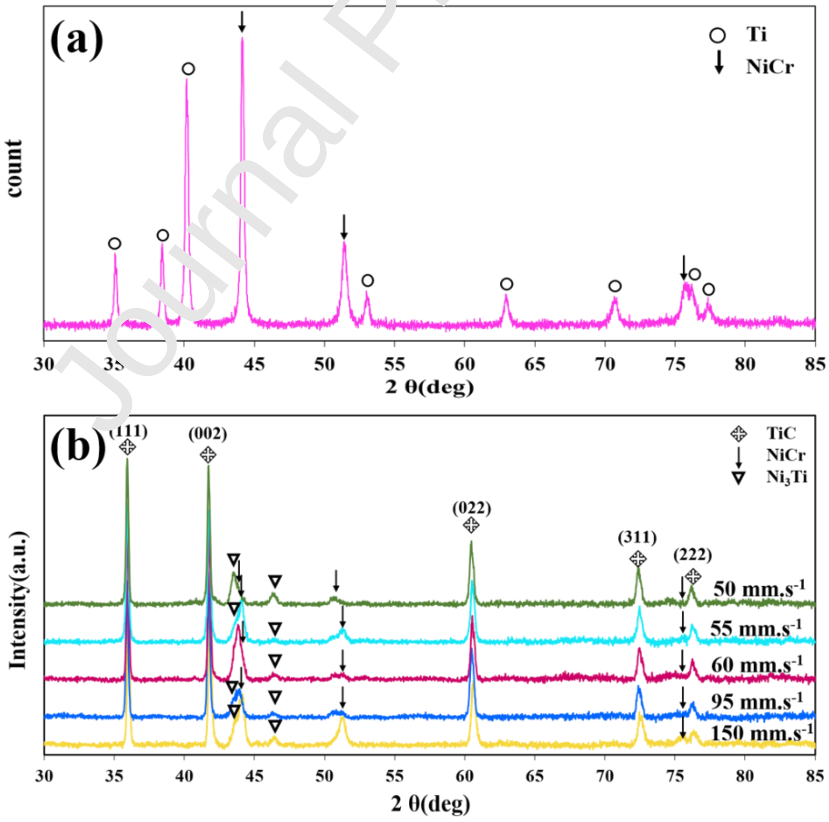

Fig. 3. XRD patterns of a) feedstock powder and b) SLM processed specimens manufactured at different scan speeds

3.2 Microstructure

Fig. 4 shows the SEM micrographs of the top surface and vertical section of the SLM samples. The dark particles correspond to the TiC phase and the white phase corresponds to the binder. At a high scan speed (150 mm.s^{-1}), melt pool and laser track are not clearly visible in the SEM image owing to insufficient melting. Moreover, due to the high heating and cooling rate, TiC particles are relatively fine (Fig. 4 a, b). As a result of decreasing the scan speed to 95 mm.s^{-1}, more visible melt pools and scan tracks were obtained and TiC particle size seems to have increased due to higher heat input. Apparently at a scan speed of 60 mm.s^{-1}, which means more heat input, adequate activation energy for pervasive Ti/C reaction is provided and more TiC can be synthesized at the initial step. Hence, more grains are produced, which leads to a finer microstructure. Lowering the scan speed to 55 mm.s^{-1} caused more melt formation and facilitated the spreading of molten material, which led to the uniform distribution of synthesized particles, reduced porosity, and increased particle size. Due to the higher heat input, the increasing trend in particle size persists with the decrease in the scan speed to 50 mm.s^{-1}.

During each pass of the printing process, the local area of the powder bed and some parts of the solidified material in the previous layer melt extremely fast [16]. When the laser beam passes over the melt pool, heat will promptly transfer to Ar atmosphere through convection and radiation, and to the layer underneath it through conduction [17]. Similar to other rapid solidification processes, during SLM process, the two competing phenomena of heterogeneous nucleation and grain growth may occur [18]. When grains are nucleated with a favorable crystallographic orientation at the liquid-solid interface, they grow quickly. Moreover, it is more likely that they will keep their crystallographic orientation during epitaxial growth. However, if the orientation of an existing grain is not the favorable crystallographic orientation, its epitaxial growth is inhibited. As a result, the solidification of the molten material arises predominantly over heterogeneous nucleation. While the epitaxial growth is dominant, a small number of large grains appear which are not limited to the melt pools. In contrast, when heterogeneous nucleation mechanisms are prevailing, a large number of small grains, confined within the melt pools, are formed. Therefore, clear laser tracks are more likely to be observed. SLM process parameters affect the thermal flux in the melt pool, which in turn influences the equilibrium of epitaxial growth and heterogeneous nucleation [19].

The dominant solidification mechanism in the present study seems to be heterogeneous nucleation. This mechanism can lead to the emergence of typical random crystallographic orientations as a result of the exothermic reaction of Ti/C. Generally, the expectation is that the exact form of the thermal flux field will be complicated on account of convection phenomena and the Marangoni effect [17]. Moreover, in the case of in situ reaction, the exothermic TiC formation reaction gives rise to complex temperature gradients in different parts of the melt pool [15]. In addition, the rotating scanning strategy (60˚ rotation in every layer) causes the appearance of irregular half ellipses (side view of melt pools) with different morphologies in consecutive layers [19]. The mismatch between layers in terms of the position of the melt pools can prevent the development of a dominant texture in the resultant sample [20].

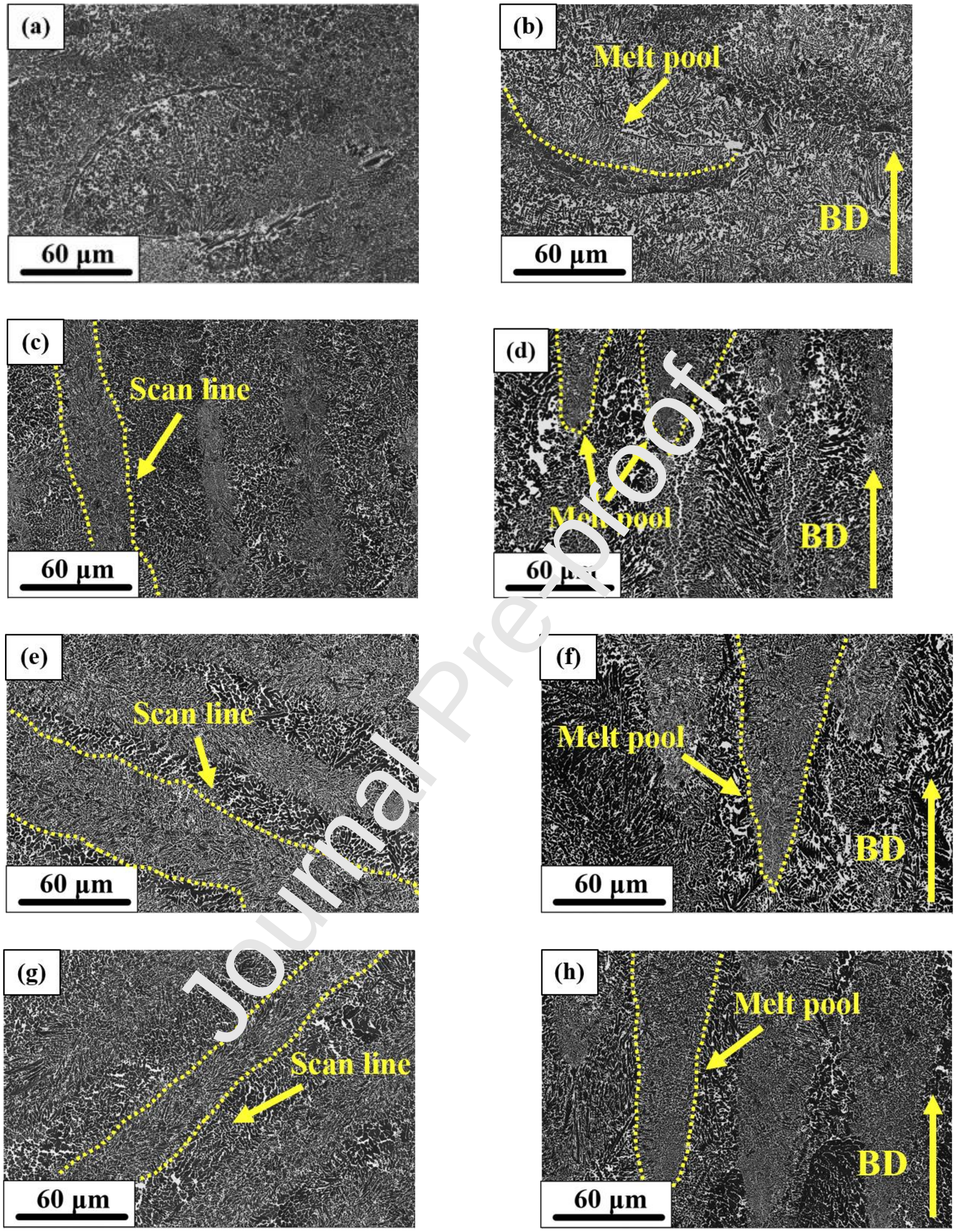
(a)
60 μm
(b)
Melt pool
BD
60 μm
(c)
Scan line
60 μm
(d)
Melt pool
BD
60 μm
(e)
Scan line
60 μm
(f)
Melt pool
BD
60 μm
(g)
Scan line
60 μm
(h)
Melt pool
BD
60 μm

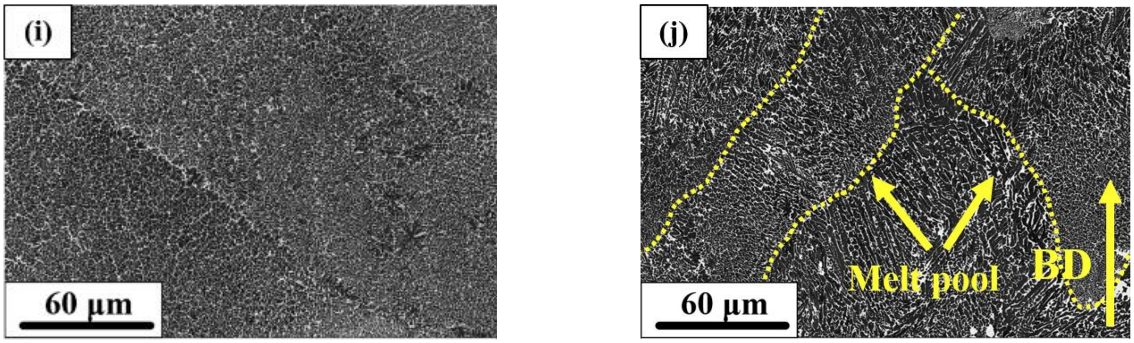

Fig. 4. SEM micrographs of top surface and longitudinal section of SLM processed specimens manufactured at different scan speeds, (a, b) 150 mm·s^{-1}, (c, d) 95 mm·s^{-1}, (e, f) 60 mm·s^{-1}, (g, h) 55 mm·s^{-1}, and (i, j) 50 mm·s^{-1}

Fig. 5 presents the normal direction crystallographic orientation maps of the horizontal and longitudinal sections of manufactured samples using TiC phase to index the EBSD patterns. Despite the fact that all SLM manufactured specimens show nearly random orientational distribution of grains, a higher concentration of one crystallographic orientation in each energy density is obvious. For both top surface and longitudinal sections, at the scan speeds of 150 mm.s^{-1} and 95 mm.s^{-1}, (111)//BD and (001)//BD orientations have been randomly distributed, respectively. At the scan speed of 60 mm.s^{-1}, (001)//BD orientation seems to be the most dominant. However, low scan speeds of 55 mm.s^{-1} and 50 mm.s^{-1} resulted in a notable difference between grain orientation on the top surface and longitudinal section. On the top surface of the sample obtained with 55 mm.s^{-1} energy density, (101)//BD can be considered as the most dominant orientation, which altered to the random distribution of (111)//BD and (101)//BD on the longitudinal section. The sample obtained with a scan speed of 50 mm.s^{-1} showed randomly distributed (001)//BD and (101)//BD orientations on the top surface that turned into (111)//BD on the longitudinal section. As previously mentioned, exothermic in situ reaction and the 60^{o}

rotation scan strategy can be considered as factors responsible for the random orientation of the grain structure. Moreover, the size of the grain structure seems to increase with decrease in the scan speed from 150 mm.s^{-1} to 95 mm.s^{-1}. At the scan speed of 60 mm.s^{-1}, finer grain structure was obtained, which can be attributed to higher Ti/C reaction rate, as mentioned in the microstructure section. Further decrease in the scan speed to 55 mm.s^{-1} and 50 mm.s^{-1} resulted in a coarser structure. Additionally, grains are more elongated in the samples obtained at the scan speeds of 55 mm.s^{-1} and 50 mm.s^{-1}. Changes in the size and shape of the grains can be explained by the increase in temperature gradient between the center and the boundary of the melt pool with decreasing scan speed (increasing laser exposure time of the powder bed). As previously mentioned, as a result of in situ reaction between Ti and C during laser scanning, the temperature gradient within the melt pool does not follow the usual patterns, which can affect the grain orientation.

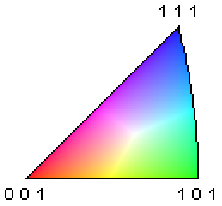

Horizontal Vertical

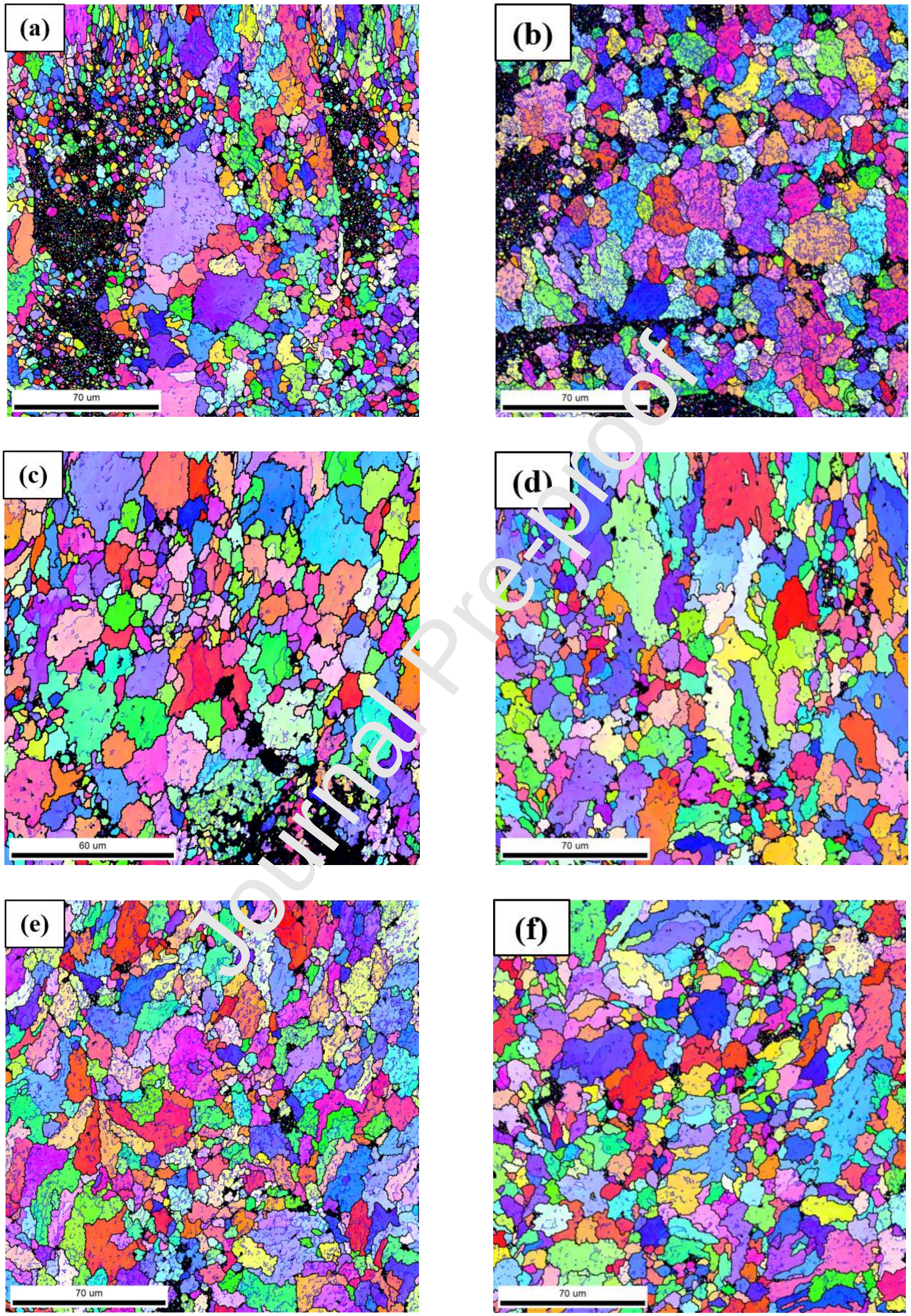
(a)
70 um
(b)
70 um
(c)
60 um
(d)
70 um
(e)
70 um
(f)
70 um

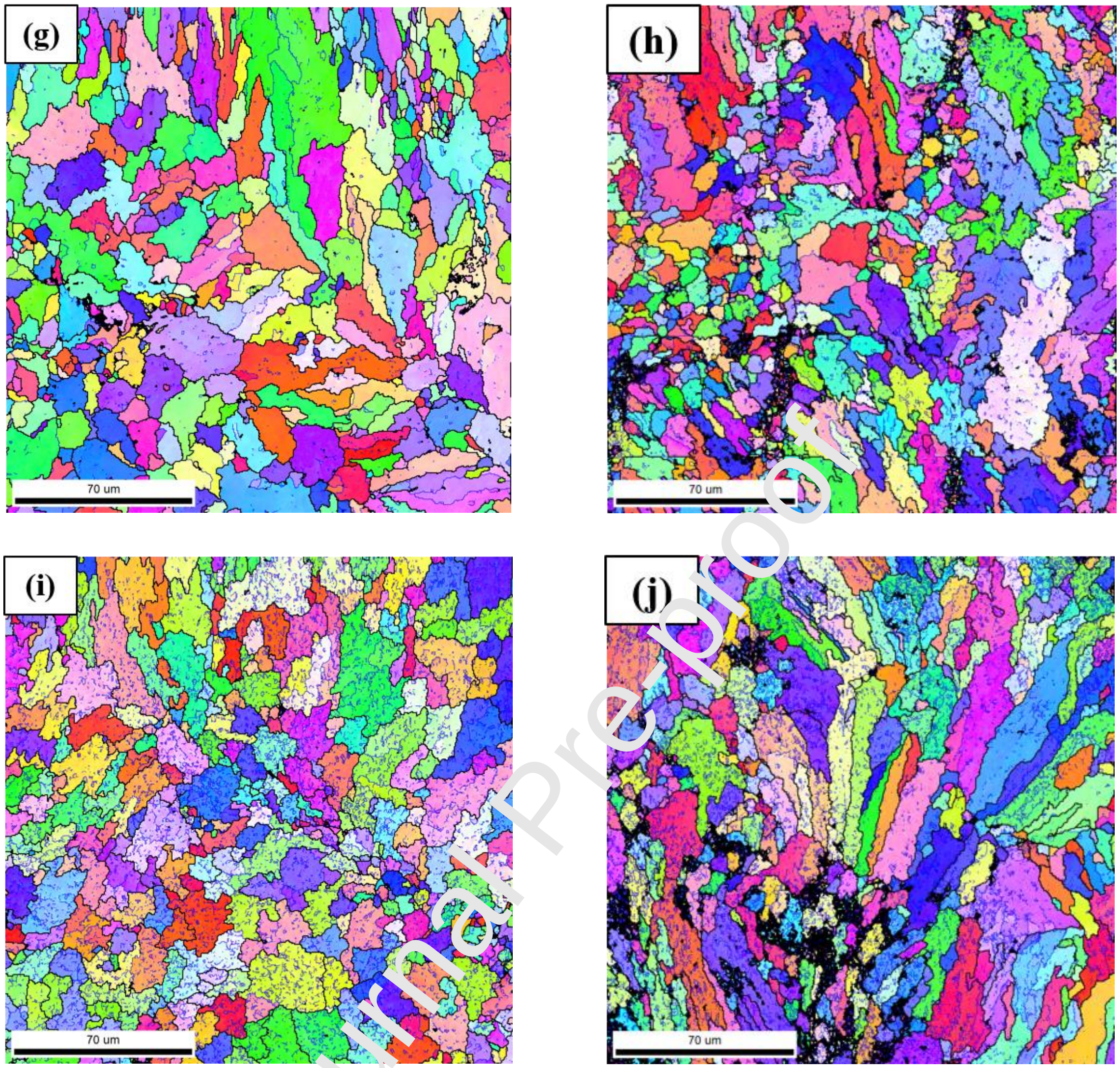

Fig. 5. BD IPF maps of the horizontal and vertical sections, (a, b) 150 mm·s^{-1}, (c, d) 95 mm·s^{-1}, (e, f) 60 mm·s^{-1}, (g, h) 55 mm·s^{-1}, and (i, j) 50 mm·s^{-1} scan speeds

The kernel average misorientation (KAM) maps are presented in Fig. 6. KAM maps can be used to study the local strains since they represent the average misorientation between a given point and its nearest neighbors. Therefore, considering the fact that plastic strain is attributed to dislocations, the density of geometrically necessary dislocations (GNDs) can be reflected by the KAM maps [21–23]. It is stated that high heating and cooling rates due to high laser scan speeds result in the accumulation of residual thermal stress [24,25], which in turn increases the dislocation density. With the reduction of scan speed, and consequently, reduction of thermal stress, the average KAM decreased in SLM processed samples. At the scan speed of 60 mm.s^{-1} (higher input energy density), a large number of initial TiC nuclei can be formed in the melt pool, which means smaller grain size and an increased number of grain boundaries. Considering the fact that grain boundaries accommodate strain and dislocations resulted from different sources such as coefficient of thermal expansion (CTE) strain mismatch between TiC and binder, the average KAM increased at 60 mm.s^{-1} scan rate. According to the KAM maps, it can be concluded that, at a scan speed of 55 mm.s^{-1}, the induced heat from each layer may have provided enough energy for recrystallization in the previously fabricated layer and the consequent reduction in dislocation density. The average KAM increased in the sample obtained with 50 mm.s^{-1} scan speed, which can be explained by increased evaporation of the elements during laser scanning as well as an increase in the sample shrinkage due to the high input energy density [26]. In addition, at lower scan speeds, and thus, higher heat inputs, the effect of the difference between the thermal expansion of TiC and NiCr binders increases, which can induce more residual stress at the TiC/NiCr interface.

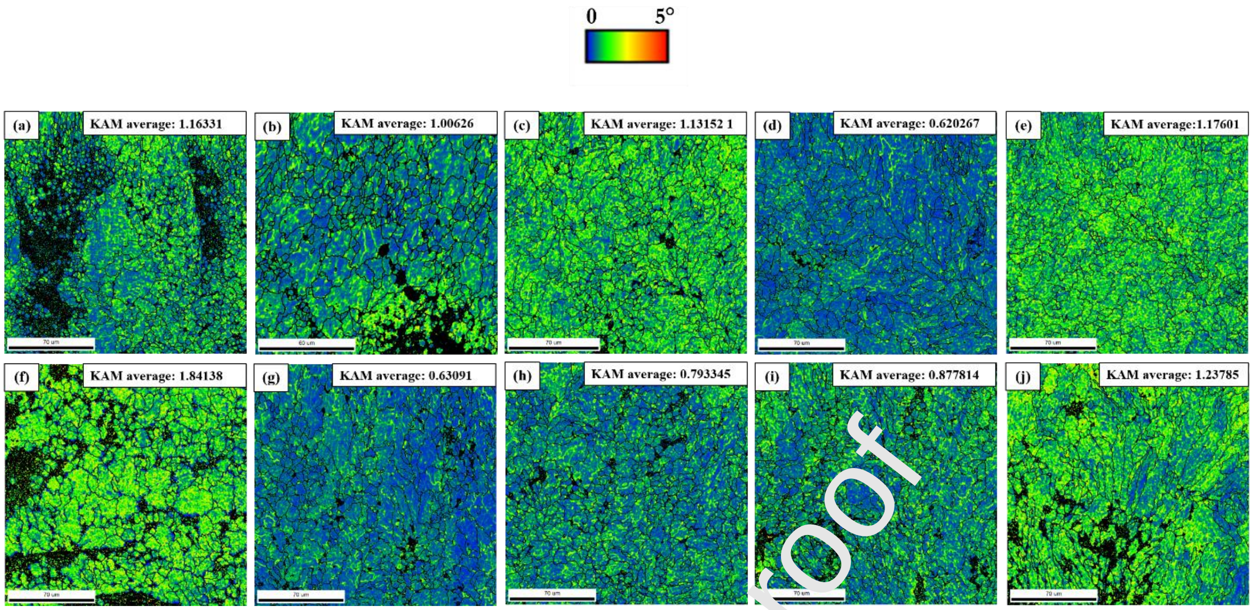
0
5°
(a)
KAM average: 1.16331
(b)
KAM average: 1.00626
(c)
KAM average: 1.13152 1
(d)
KAM average: 0.620267
(e)
KAM average:1.17601
(f)
KAM average: 1.84138
(g)
KAM average: 0.63091
(h)
KAM average: 0.793345
(i)
KAM average: 0.877814
(j)
KAM average: 1.23785

Fig. 6. KAM maps of the horizontal and vertical section at (a, f) 150 mm·s^{-1}, (b, g) 95 mm·s^{-1}, (c, h) 60 mm·s^{-1}, (d, i) 55 mm·s^{-1}, and (e, j) 50 mm·s^{-1} scan speeds

Figures 7 and 8 show the misorientation angle distribution and the grain boundary maps on the top and longitudinal sections of SLM manufactured specimens, respectively. The boundaries are color-coded with low angle grain boundaries (LAGBs) (θ < 15°) in blue and high angle grain boundaries (HAGBs) (θ > 15°) in black. Due to rapid melting and solidification as well as thermal gradients during the SLM process, dislocation walls are formed by the interaction of dislocations, which results in a high fraction of sub-grains. Throughout the scanning of each layer, the previous layer is re-heated, and the induced heat causes recrystallization and formation of HAGBs [27]. However, due to the rapid cooling rates during the SLM process, based on the applied scan speed, some residual LAGBs remain in the microstructure of the manufactured samples [28,29]. The majority of grain boundaries in both the longitudinal section and top surface of SLM manufactured specimens are characterized as HAGBs (with some exceptions, especially at 150 mm.s^{-1} (top surface) related to the presence of non-indexed areas (which mostly includes printing defects such as pores, unmolten particles, and very fine grains). It is well known that the toughness of a material can be attributed to the fraction of HAGBs in the structure since they can hinder crack propagation. Moreover, higher misorientation angle of adjacent grain boundaries leads to increased ability of the material to resist crack propagation [30]. Hence, if only the effect of grain boundary misorientation is considered, the highest toughness value can be expected in the sample containing the highest fraction of HAGBs. As previously reported, the sample obtained at the scan speed of 55 mm.s^{-1} showed the highest fracture toughness value of 25.9 MPa.m$^{1/2}$ and the sample manufactured at the scan speed of 150 mm.s^{-1} showed the lowest value (18.88 MPa.m$^{1/2}$) [15]. Although various factors affect fracture toughness (grain size, defects, and uniform distribution of grain), the higher fraction of HAGBs on the surface of the sample manufactured at 55 mm.s^{-1} can explain the improvement of fracture toughness.

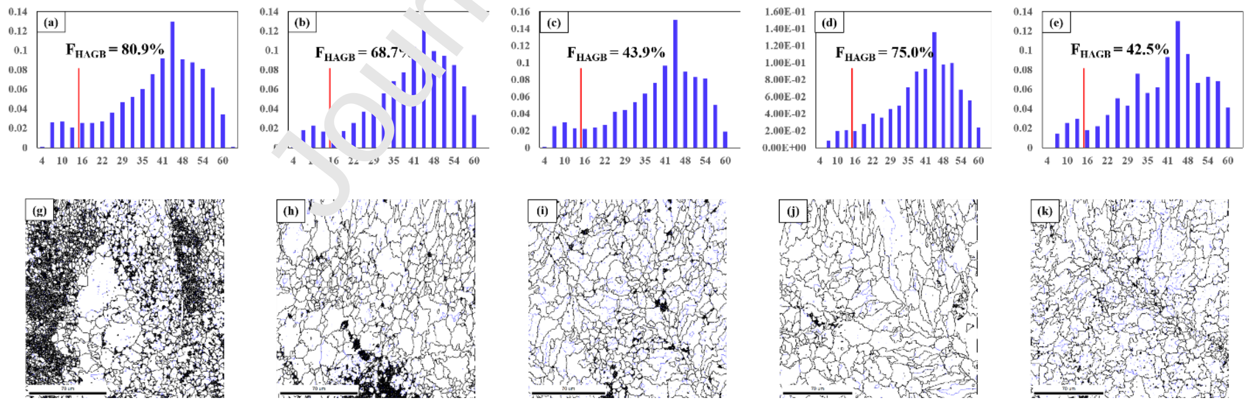

Fig. 7. Grain boundary misorientation distribution profiles and grain boundary maps obtained from the top surface of the SLM manufactured samples with different scan speeds, (a, g) 150 mm·s^{-1}, (b, h) 95 mm·s^{-1}, (c, i) 60 mm·s^{-1}, (d, j) 55 mm·s^{-1}, and (e, k) 50 mm·s^{-1}

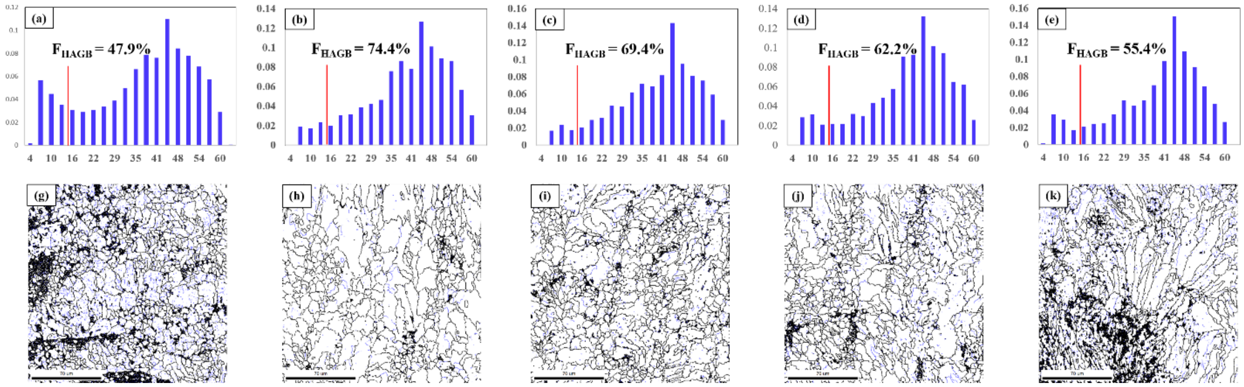

Fig. 8. Grain boundary misorientation distribution profiles and grain boundary maps obtained from the logitudinal section of SLM manufactured samples at different scan speeds, (a, g) 150 mm·s^{-1}, (b, h) 95 mm·s^{-1}, (c, i) 60 mm·s^{-1}, (d, j) 55 mm·s^{-1}, and (e, k) 50 mm·s^{-1}

3.3 Texture evaluation

3.3.1 X-ray analysis

Macrotexture measurements were conducted to investigate the effect of SLM process on texture formation. Pole figures and orientation distribution function (ODF) maps of SLM manufactured samples are shown in Fig. 9. The ideal texture components of face center cubic (FCC) material are presented in Table 1. It seems that fiber textures have developed during SLM at different scan speeds. Moreover, as shown in the ODF maps, Cube, Goss, and Brass can be considered as the main texture components in the specimens.

Table. 1. The ideal texture components of FCC material [31]

Texture component	Symbol	Euler angles			Miller indices	Fiber
		Φ_1/°	ϕ/°	Φ_2/°		
Cube(C)	□	45	0	45	{001}<100>	-
Goss(G)	▭	90	90	45	{110}<001>	α/τ
Brass(B)	⬭	55	90	45	{110}<112>	α/β

Copper(Cu)	⧗	90	35	45	{112}<111>	τ/β
G/B	⬡	74	90	45	{110}<115>	α
Rotated cube (Rt-C)	◇	0/90	0	45	{001}<110>	τ
Rotate Goss (Rt-G)	▯	0	90	45	{011}<011>	α
A	⬯	35	90	45	{110}<111>	α
F	⇧	30/90	55	45	{111}<112>	γ/τ
E	⇩	0/60	55	45	{111}<011>	γ
Rotate copper	☾	0	35	45	{112}<011>	τ/β

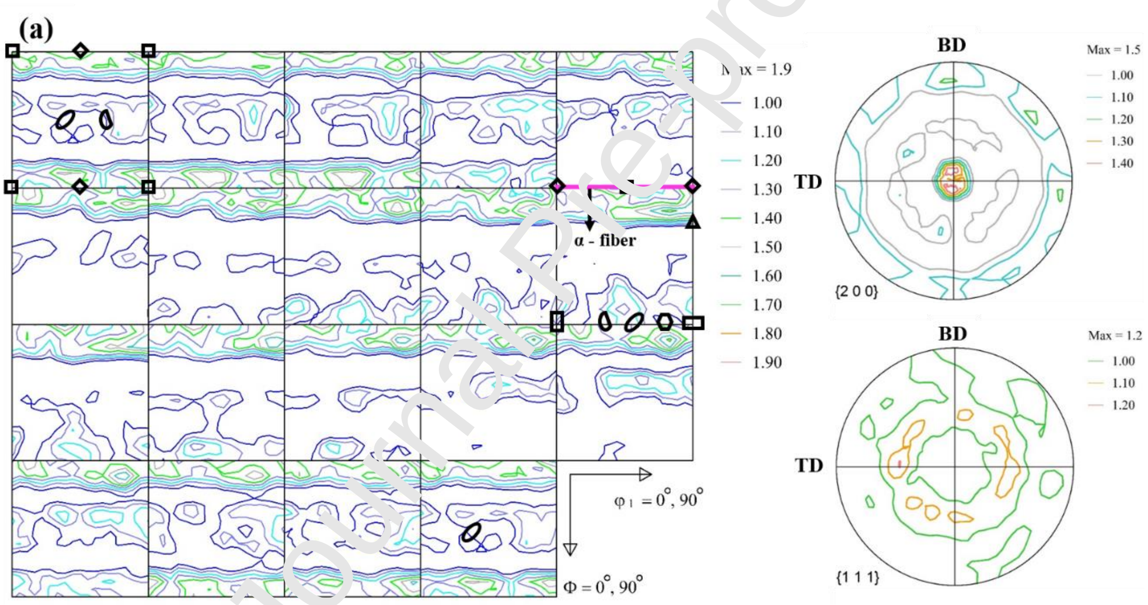

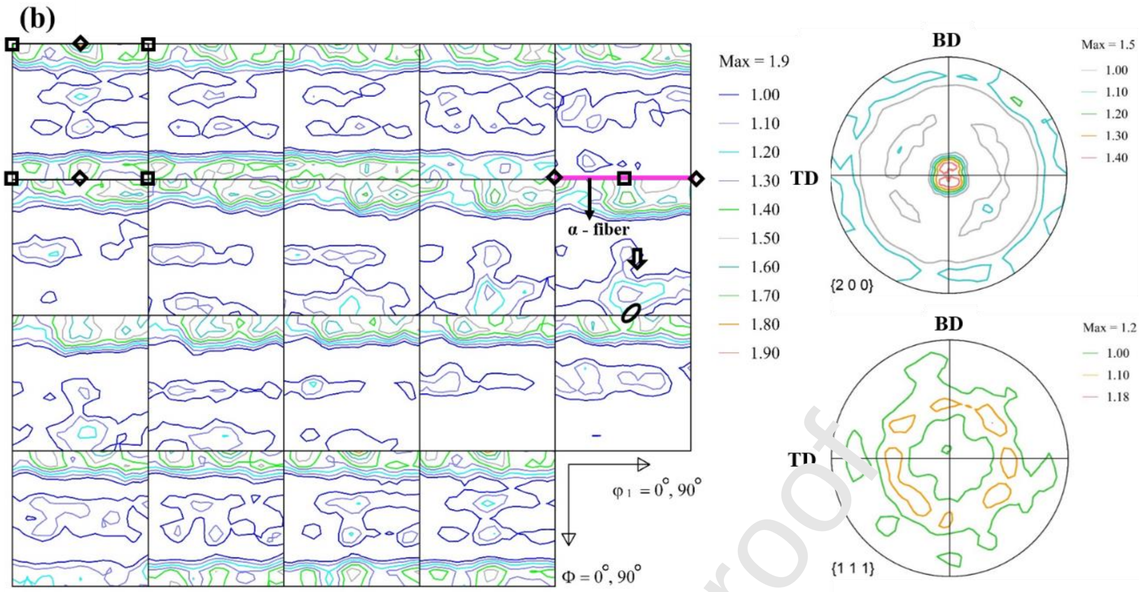
(b)
Max = 1.9
1.00
1.10
1.20
1.30
1.40
1.50
1.60
1.70
1.80
1.90
α - fiber
φ1 = 0°, 90°
Φ = 0°, 90°
BD
TD
{2 0 0}
Max = 1.5
1.00
1.10
1.20
1.30
1.40
BD
TD
{1 1 1}
Max = 1.2
1.00
1.10
1.18

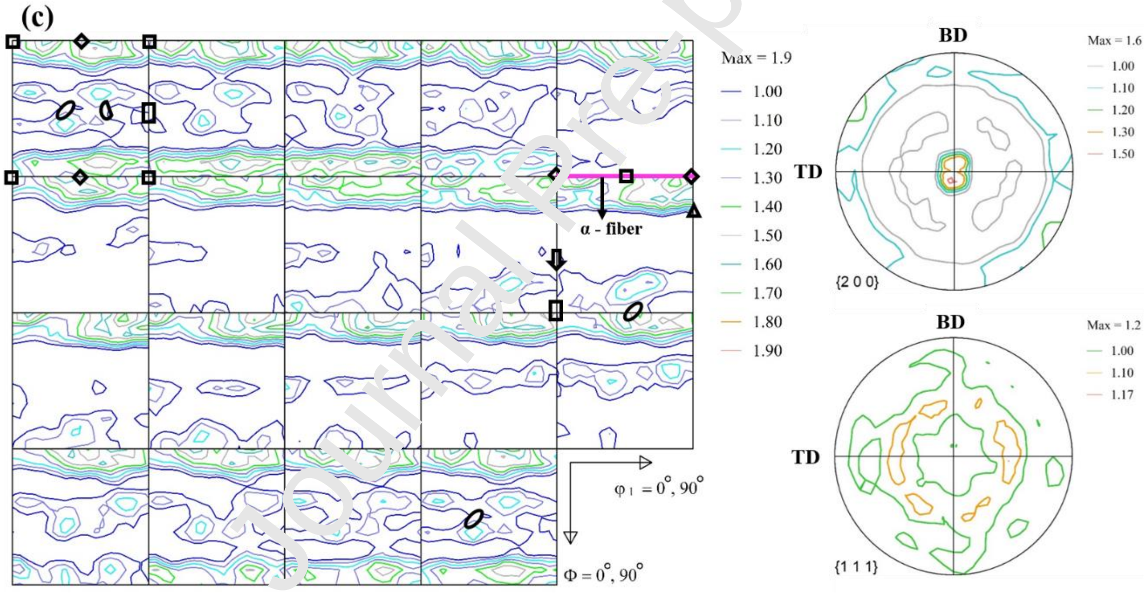
(c)
Max = 1.9
1.00
1.10
1.20
1.30
1.40
1.50
1.60
1.70
1.80
1.90
α - fiber
φ1 = 0°, 90°
Φ = 0°, 90°
BD
TD
{2 0 0}
Max = 1.6
1.00
1.10
1.20
1.30
1.50
BD
TD
{1 1 1}
Max = 1.2
1.00
1.10
1.17

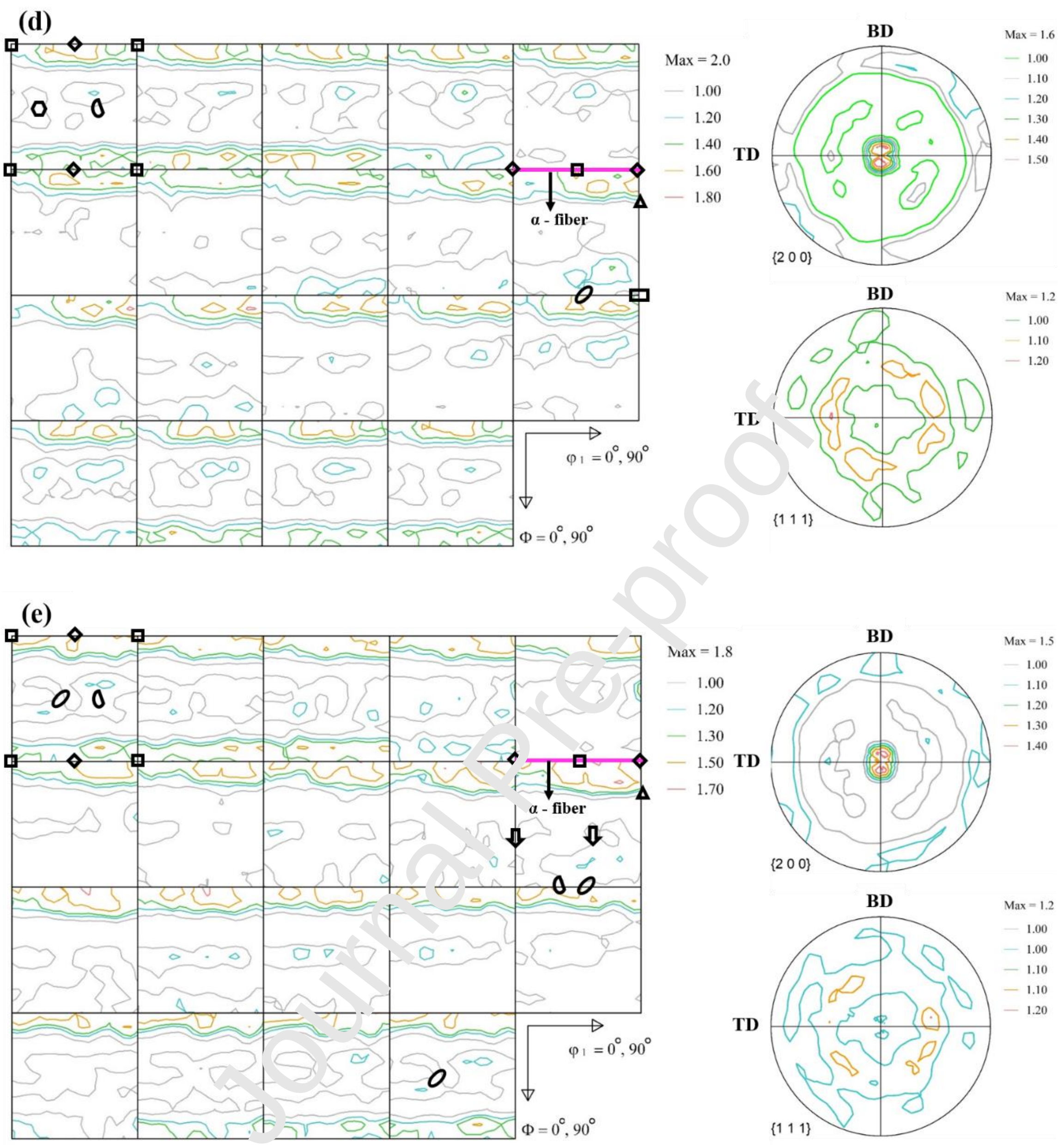

Fig. 9. Macroanalyses of ODF maps and pole figures of the longitudinal section of SLM processed specimens manufactured at different scan speeds, (a) 150 mm·s^{-1}, (b) 95 mm·s^{-1}, (c) 60 mm·s^{-1}, (d) 55 mm·s^{-1}, and (e) 50 mm·s^{-1}

3.3.2 EBSD analysis

ODF and pole figures of the longitudinal section of SLM manufactured samples are shown in Fig. 10. ODF and pole figures do not show obvious dominating textures in SLM manufactured cermets, but some relatively weak components can be observed. All samples show stronger texture intensity in (001) pole figures compared to other orientations in the normal direction (i.e., radial direction). However, the maximum texture intensities in pole figures are roughly 2.14, 3.70, 2.12, 3.38, and 2.83 (versus random texture), which can be considered random. This lack of dominant texture in EBSD analyses can be illustrated by the non-uniform temperature gradient in the melt pool due to the nucleation of TiC through exothermic in situ reaction between Ti and C in the different parts of the melt pool as well as the 60° rotation scan strategies, which leads to the absence of a preferred direction of solidification.

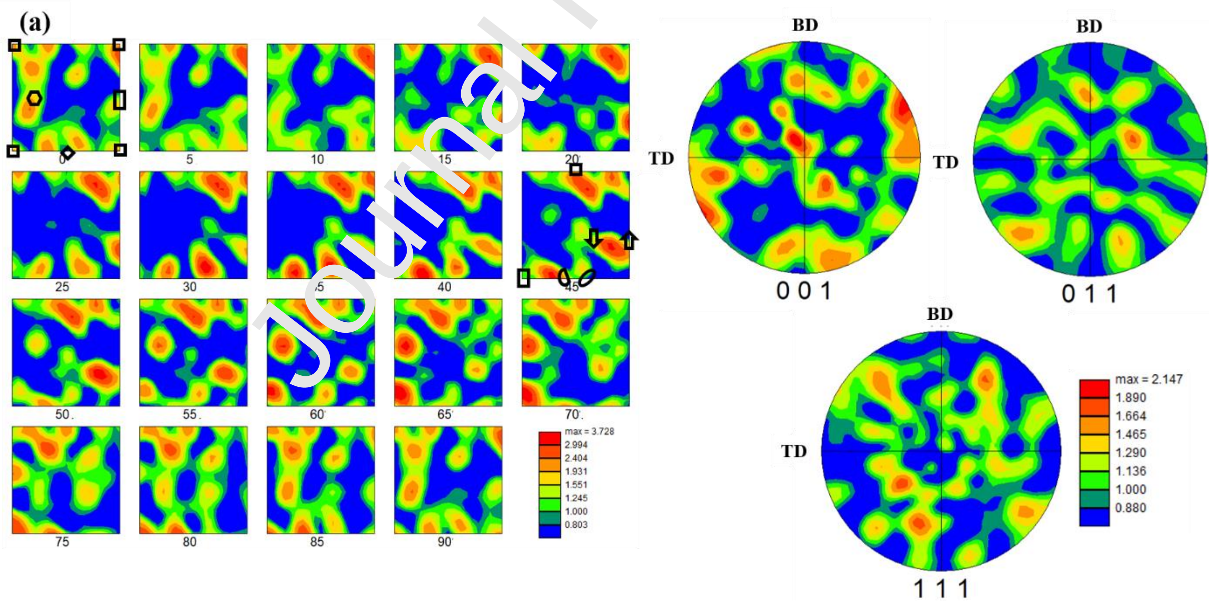

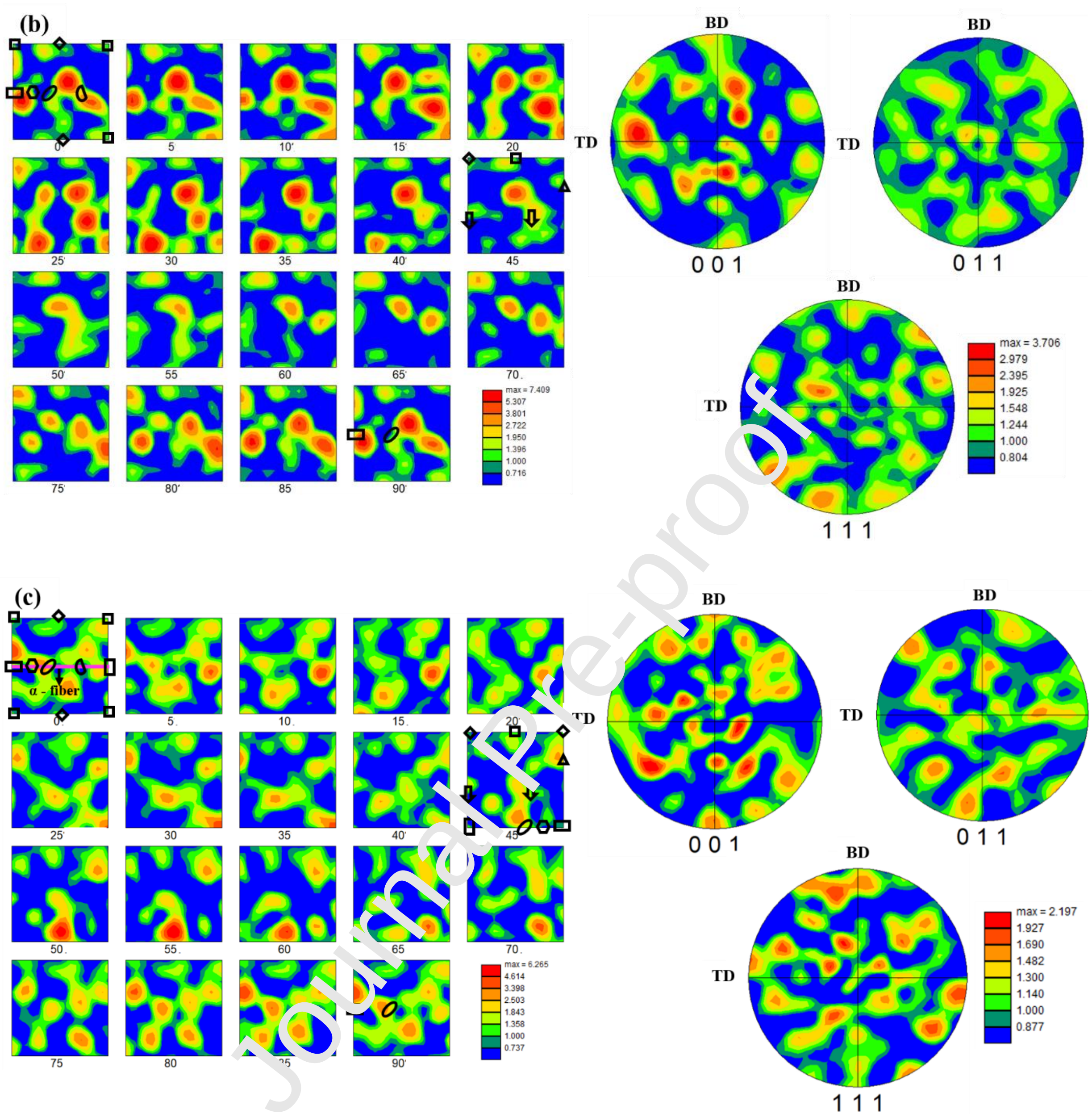
(b)
0
5
10
15
20
25
30
35
40
45
50
55
60
65
70
75
80
85
90
max = 7.409
5.307
3.801
2.722
1.950
1.396
1.000
0.716
BD
TD
0 0 1
BD
TD
0 1 1
BD
TD
1 1 1
max = 3.706
2.979
2.395
1.925
1.548
1.244
1.000
0.804
(c)
α - fiber
0
5
10
15
20
25
30
35
40
45
50
55
60
65
70
75
80
85
90
max = 6.265
4.614
3.398
2.503
1.843
1.358
1.000
0.737
BD
TD
0 0 1
BD
TD
0 1 1
BD
TD
1 1 1
max = 2.197
1.927
1.690
1.482
1.300
1.140
1.000
0.877

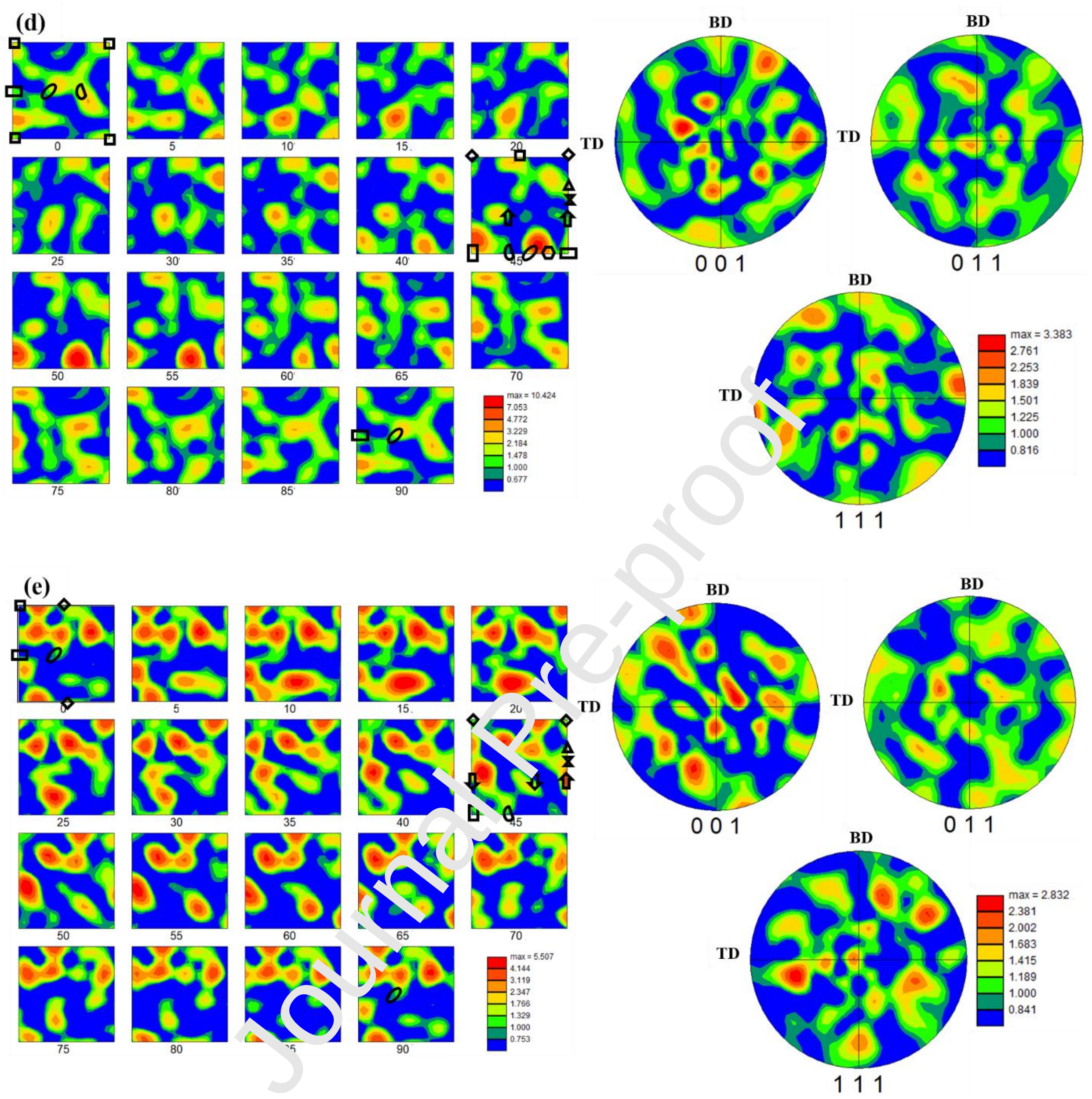

Fig. 10. ODF maps and pole figures of longitudinal sections of SLM processed specimens manufactured at different scan speeds, (a) 150 $\mathrm{mm\cdot s^{-1}}$, (b) 95 $\mathrm{mm\cdot s^{-1}}$, (c) 60 $\mathrm{mm\cdot s^{-1}}$, (d) 55 $\mathrm{mm\cdot s^{-1}}$, and (e) 50 $\mathrm{mm\cdot s^{-1}}$

Fig. 11 shows the inverse pole figure (IPF) charts obtained from EBSD analysis on the top surface of SLM manufactured specimens. Similar to the longitudinal section, there is no sign of dominant texture on the top surface. The maximum intensity is relatively low in all of the samples (from 1.286 to 2.196 versus random texture). In the specimens manufactured at scan speeds of 150 mm·s^{-1} and 95 mm·s^{-1}, the detected points have accumulated between (001)//BD and (111)//BD directions. Points have accumulated at (001)//BD in the sample manufactured at a scan speed of 60 mm·s^{-1} and (101)//BD in the samples manufactured at scan speeds of 55 mm·s^{-1} and 50 mm·s^{-1}.

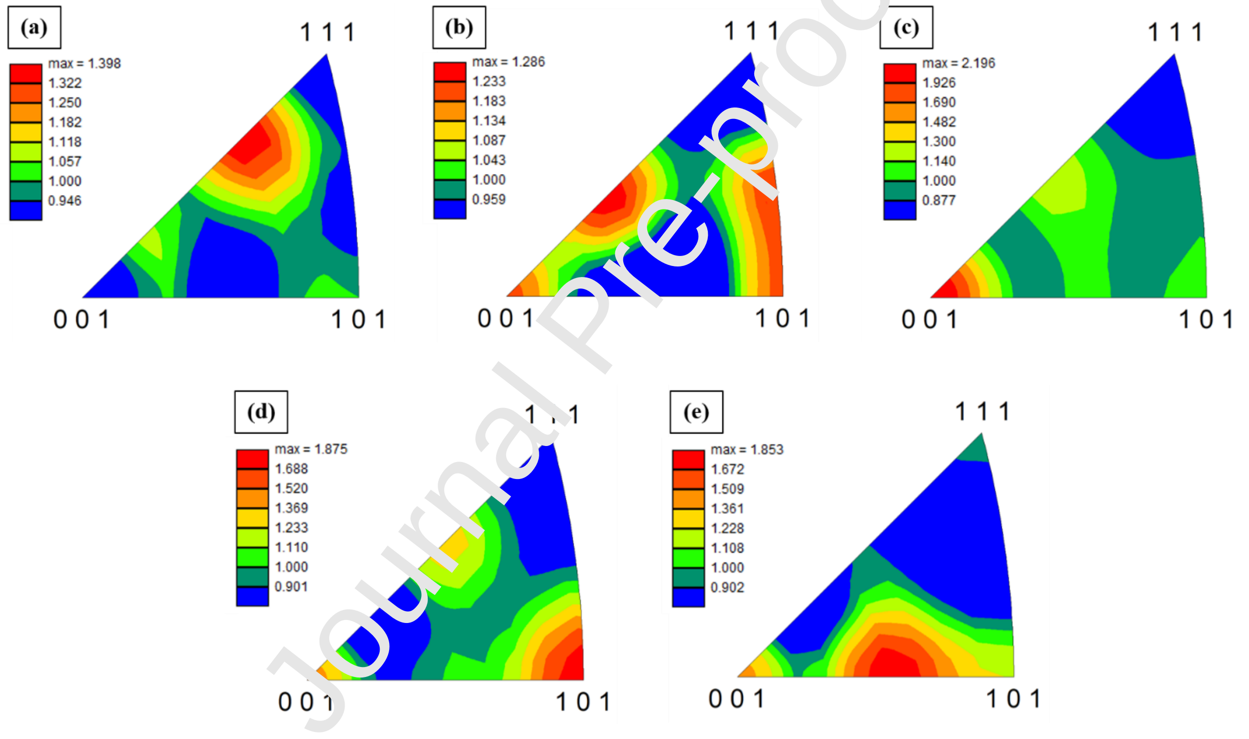

Fig. 11. BD IPFs of SLM processed specimens manufactured at different scan speeds, (a) 150 mm·s^{-1}, (b) 95 mm·s^{-1}, (c) 60 mm·s^{-1}, (d) 55 mm·s^{-1}, and (e) 50 mm·s^{-1}

3.2.3 Schmid factor

Figs. 12-13 show the distribution of grain orientation relative to building direction in the form of Schmid factors on the top surface and longitudinal section of the manufactured specimens. It has been acknowledged that the plastic deformation ability of a material can be characterized by its Schmid factor [32]. Plastic deformation arises when the resolved shear stress in the slip plane and slip direction reaches the crucial value. Therefore, according to the following formula, higher Schmid factors lead to lower yield stress and higher toughness and ductility [33,34].

$$\tau_C = \delta_s \cos\lambda \ \cos\emptyset$$

$\cos\lambda \cos\emptyset$ is the Schmid factor (SF), τ_c is the intrinsic coefficient of materials, which is determined by the material itself, and σ_s is the yield strength of the material.

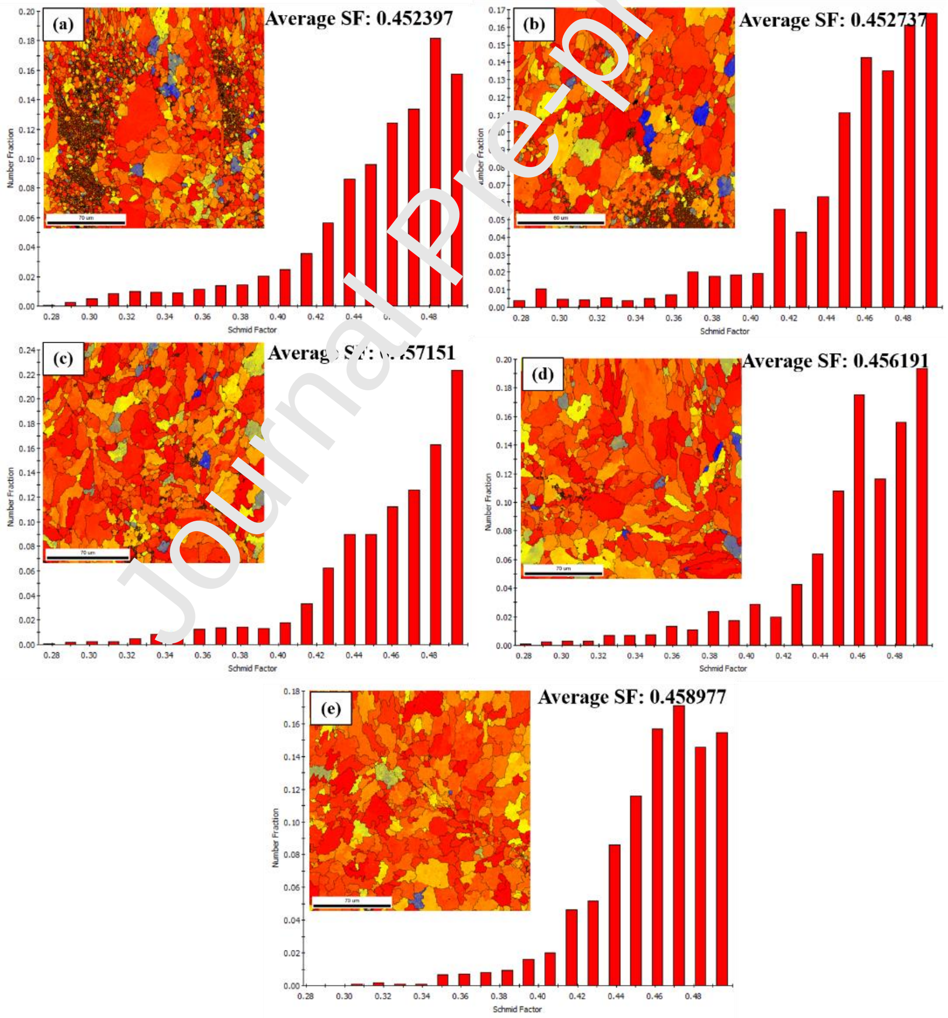

Fig. 12. Schmid factor maps and distribution profiles of the top surface of SLM processed samples manufactured at different scan speeds, (a) 150 mm·s^{-1}, (b) 95 mm·s^{-1}, (c) 60 mm·s^{-1}, (d) 55 mm·s^{-1}, and (e) 50 mm·s^{-1}

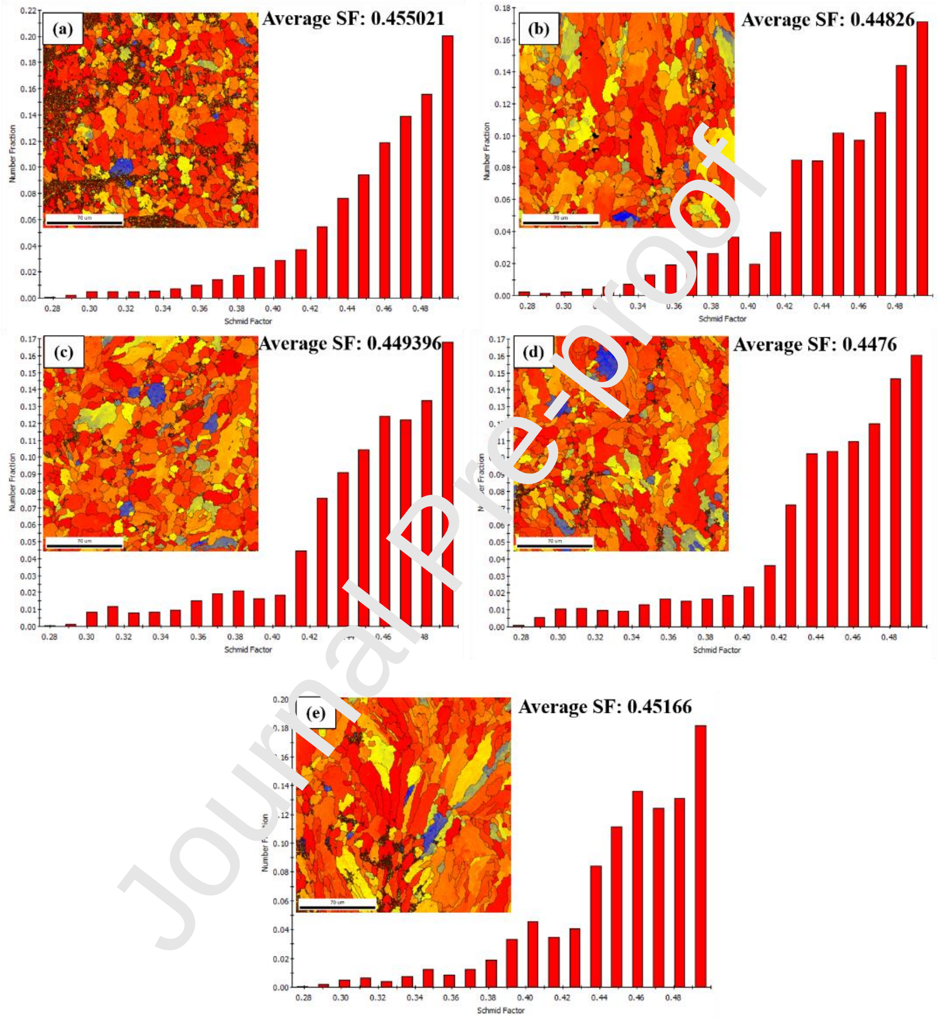

Fig. 13. Schmid factor maps and distribution profiles of the longitudinal section of SLM processed samples manufactured at different scan speeds, (a) 150 mm·s^{-1}, (b) 95 mm·s^{-1}, (c) 60 mm·s^{-1}, (d) 55 mm·s^{-1}, and (e) 50 mm·s^{-1}

4. Conclusion

1. Among the two possible solidification phenomena (heterogeneous nucleation and epitaxial growth), heterogeneous nucleation is proposed to possess the dominant role during solidification.
2. Rotation scan strategy and exothermic in situ reaction seemed to be responsible for the near random texture, and α-fiber was the obvious texture in ODF maps of microtexture and macrotexture analyses.
3. KAM distribution maps revealed the lowest average KAM in the sample manufactured at a scan speed of 55 mm·s^{-1}, considering both top surface and longitudinal sections of the SLM samples; this means that the lowest thermal strain and number of dislocations were obtained in the sample produced with this scanning speed.

Aknowledgement

The present research was supported by Shahid Chamran University of Ahvaz under grant number GN26247.

Conflict of Interest

All authors declare that there is no conflict of interest regarding the publication of this article. All authors have participated in (a) fabrication, or analysis and interpretation of the data, writing and revising paper critically for important intellectual content; (b) sample analyzing and revising paper critically for important intellectual content; and (c) sample fabrication.

References

[1] N. Yang, Y. Tian, D. Zhang, Novel real function based method to construct heterogeneous porous scaffolds and additive manufacturing for use in medical engineering, Med. Eng. Phys. 37 (2015) 1037–1046. doi:10.1016/j.medengphy.2015.08.006.

[2] B. Song, S. Dong, P. Coddet, H. Liao, C. Coddet, Fabrication of NiCr alloy parts by selective laser melting : Columnar microstructure and anisotropic mechanical behavior, J. Mater. 53 (2014) 1–7. doi:10.1016/j.matdes.2013.07.010.

[3] T. Niendorf, S. Leuders, A. Riemer, H.A. Richard, D. Schwarze, Highly Anisotropic Steel Processed by Selective Laser Melting by Selective Laser Melting, Metall. Mater. Trans. B. 44 (2013) 794–796. doi:10.1007/s11663-013-9875-z.

[4] L. Thijs, M.L. Montero-sistiaga, R. Wauthle, Q. Xie, Strong morphological and crystallographic texture and resulting yield strength anisotropy in selective laser melted tantalum, Acta Mater. 61 (2013) 4657–4668. doi:10.1016/j.actamat.2013.04.036.

[5] A. Aramian, S.M.J. Razavi, Z. Sadeghian, K.G. Prashanth, F. Berto, A review of additive manufacturing of cermets, Addit. Manuf. 33 (2020) 101130. doi:10.1016/j.addma.2020.101130.

[6] A. Aramian, Z. Sadeghian, P. Konda Gokuldoss, F. Berto, In situ fabrication of TiC-NiCr cermets by selective laser melting, Int. J. Refract. Met. Hard Mater. 87 (2020) 105171. doi:10.1016/j.ijrmhm.2019.105171.

[7] C. Jin, C.C. Onuoha, Z.N. Farhat, G.J. Kipouros, K.P. Plucknett, Reciprocating wear behaviour of TiC-stainless steel cermets, Tribol. Int. (2017).

doi:10.1016/j.triboint.2016.10.012.

[8] C. Jin, C.C. Onuoha, Z.N. Farhat, G.J. Kipouros, K.P. Plucknett, Microstructural damage following reciprocating wear of TiC-stainless steel cermets, Tribol. Int. 105 (2017) 201–218. doi:10.1016/j.triboint.2016.10.011.

[9] S. Okamoto, Y. Nakazono, K. Otsuka, Y. Shimoitani, J. Takada, Mechanical properties of WC/Co cemented carbide with larger WC grain size, Mater. Charact. 55 (2005) 281–287. doi:https://doi.org/10.1016/j.matchar.2005.06.001.

[10] V.B. Voitovich, V. V. Sverdel, R.F. Voitovich, E.I. Golovko, Oxidation of WC-Co, WC-Ni and WC-Co-Ni Hard Metals in the Temperature Range 500-800°C, Int. J. Refract. Met. Hard Mater. 14 (1996) 289–295. doi:10.1016/0263-4368(96)00009-1.

[11] M. Mathapati, M.R. Ramesh, M. Doddamani, High temperature erosion behavior of plasma sprayed NiCrAlY/WC-Co/cenosphere coating, Surf. Coatings Technol. 325 (2017) 98–106. doi:10.1016/j.surfcoat.2017.06.033.

[12] J. Kübarsepp, H. Klaasen, J. Pirso, Behavior of TiC-base cermets in different wear conditions, Wear. 249 (2001) 229–234. doi:10.1016/S0043-1648(01)00569-5.

[13] I. Hussainova, Effect of microstructure on the erosive wear of titanium carbide-based cermets, Wear. 255 (2003) 121–128. doi:10.1016/S0043-1648(03)00198-4.

[14] O. R. Engler, Introduction to Texture Analysis. Macrotexture, Microtexture, and Orientation Mapping, 2014.

[15] A. Aramian, Z. Sadeghian, S.M.J. Razavi, K.G. Prashanth, F. Berto, Effect of selective laser melting process parameters on microstructural and mechanical properties of TiC–

NiCr cermet, Ceram. Int. (2020). doi:10.1016/j.ceramint.2020.08.037.

[16] V.A. Popovich, E. V. Borisov, A.A. Popovich, V.S. Sufiiarov, D. V. Masaylo, L. Alzina, Functionally graded Inconel 718 processed by additive manufacturing: Crystallographic texture, anisotropy of microstructure and mechanical properties, Mater. Des. 114 (2017) 441–449. doi:10.1016/j.matdes.2016.10.075.

[17] M. Xia, D. Gu, G. Yu, D. Dai, H. Chen, Q. Shi, Selective laser melting 3D printing of Ni-based superalloy: understanding thermodynamic mechanisms, Sci. Bull. 61 (2016) 1013–1022. doi:10.1007/s11434-016-1098-7.

[18] S. Kou, Welding Metallurgy, 2003. doi:10.22486/iwj.v4i3.150243.

[19] M. Calandri, S. Yin, B. Aldwell, F. Calignano, R. Lupoi, D. Ugues, Texture and microstructural features at different length scales in Inconel 718 produced by selective laser melting, Materials (Basel). 12 (2019). doi:10.3390/ma12081293.

[20] S. Sun, K. Hagihara, T. Nakano, Effect of scanning strategy on texture formation in Ni-25 at .% Mo alloys, Mater. Des. 140 (2018) 307–316. doi:10.1016/j.matdes.2017.11.060.

[21] S.I. Wright, M.M. Nowell, D.P. Field, A review of strain analysis using electron backscatter diffraction, Microsc. Microanal. 17 (2011) 316–329. doi:10.1017/S1431927611000055.

[22] D. Raabe, Texture and microstructure evolution during cold rolling of a strip cast and of a hot rolled austenitic stainless steel, Acta Mater. 45 (1997) 1137–1151. doi:10.1016/S1359-6454(96)00222-4.

[23] H.P. Lin, T.S. Ng, J.C. Kuo, Y.C. Chen, C.L. Chen, S.X. Ding, EBSD study on

crystallographic texture and microstructure development of cold-rolled FePd alloy, Mater. Charact. 93 (2014) 163–172. doi:10.1016/j.matchar.2014.04.006.

[24] F. Liu, X. Lin, G. Yang, M. Song, J. Chen, W. Huang, Microstructure and residual stress of laser rapid formed Inconel 718 nickel-base superalloy, Opt. Laser Technol. 43 (2011) 208–213. doi:10.1016/j.optlastec.2010.06.015.

[25] I. Toda-Caraballo, J. Chao, L.E. Lindgren, C. Capdevila, Effect of residual stress on recrystallization behavior of mechanically alloyed steels, Scr. Mater. 62 (2010) 41–44. doi:10.1016/j.scriptamat.2009.09.023.

[26] D. Dai, D. Gu, Tailoring surface quality through mass and momentum transfer modeling using a volume of fluid method in selective laser melting of TiC/AlSi10Mg powder, Int. J. Mach. Tools Manuf. 88 (2015) 95–107. doi:10.1016/j.ijmachtools.2014.09.010.

[27] B. AlMangour, D. Grzesiak, J.M. Yang, Scanning strategies for texture and anisotropy tailoring during selective laser melting of TiC/316L stainless steel nanocomposites, J. Alloys Compd. 728 (2017) 424–435. doi:10.1016/j.jallcom.2017.08.022.

[28] W. Li, J. Liu, Y. Zhou, S. Wen, Q. Wei, C. Yan, Y. Shi, Effect of substrate preheating on the texture, phase and nanohardness of a Ti-45Al-2Cr-5Nb alloy processed by selective laser melting, Scr. Mater. 118 (2016) 13–18. doi:10.1016/j.scriptamat.2016.02.022.

[29] Y. Zhou, X. Zeng, Z. Yang, H. Wu, Effect of crystallographic textures on thermal anisotropy of selective laser melted Cu-2.4Ni-0.7Si alloy, J. Alloys Compd. 743 (2018) 258–261. doi:10.1016/j.jallcom.2018.01.335.

[30] S. Wen, K. Chen, W. Li, Y. Zhou, Q. Wei, Y. Shi, Selective laser melting of reduced

graphene oxide/S136 metal matrix composites with tailored microstructures and mechanical properties, Mater. Des. 175 (2019) 107811. doi:10.1016/j.matdes.2019.107811.

[31] N. Eftekhari, A. Zarei-Hanzaki, A. Shamsolhodaei, A.L. Helbert, T. Baudin, Microstructural evolution and texture analysis in a thermomechanically processed low SFE super-austenitic steel (alloy-28), Adv. Eng. Mater. 20 (2018) 1–12. doi:10.1002/adem.201700928.

[32] M. Simonelli, Y.Y. Tse, C. Tuck, Effect of the build orientation on the mechanical properties and fracture modes of SLM Ti-6Al-4V, Mater. Sci. Eng. A. 616 (2014) 1–11. doi:10.1016/j.msea.2014.07.086.

[33] Z. Chen, S. Chen, Z. Wei, L. Zhang, P. Wei, B. Lu, S. Zhang, Y. Xiang, Anisotropy of nickel-based superalloy K418 fabricated by selective laser melting, Prog. Nat. Sci. Mater. Int. 28 (2018) 496–504. doi:10.1016/j.pnsc.2018.07.001.

[34] K. Li, L. Wei, B. An, B. Yu, R.D.K. Misra, Aging phenomenon in low lattice-misfit cobalt-free maraging steel: Microstructural evolution and strengthening behavior, Mater. Sci. Eng. A. 739 (2019) 445–454. doi:10.1016/j.msea.2018.10.069.

Highlights

- The exothermic Ti /C reaction changes the temperature gradient in the melt pool.
- Heterogeneous nucleation was proposed to possess the dominant role during solidification.
- In-situ TiC reaction and 60˚ rotation scan strategy affects the texture evolution during the SLM process
- The micro and macro texture of manufacture specimens was nearly random